


Coexistence of topological edge states and skin effects in the non-Hermitian Su-Schrieffer-Heeger model with long-range nonreciprocal hopping in topoelectric realizations

Ke Xu,^{1,*} Xintong Zhang,^{1,*} Kaifa Luo,² Rui Yu,^{2,†} Dan Li,³ and Hao Zhang^{1,‡}

¹Key Laboratory of Micro and Nano Photonic Structures (MOE), Department of Optical Science and Engineering, Fudan University, Shanghai 200433, China

²School of Physics and Technology, Wuhan University, Wuhan 430072, China

³Department of Electronic Engineering, Fudan University, Shanghai 200433, China

 (Received 29 October 2020; revised 24 January 2021; accepted 25 February 2021; published 10 March 2021)

Recently, the topological phase in non-Hermitian systems has been a rapidly expanding field. The iconic features of non-Hermitian systems are exceptional points at which the eigenmodes coalesce and the non-Hermitian skin effect. We study the non-Hermitian Su-Schrieffer-Heeger model with long-range nonreciprocal hopping and find the model exhibiting topologically nontrivial phases which can be characterized by the non-Bloch winding number. With specific parameter values, the skin effect can be eliminated. As long-range nonreciprocal hopping is not easy for experimental implementations, we furthermore propose a feasible electrical-circuit simulation with operational amplifiers to implement the non-Hermitian term to realize these interesting states.

DOI: [10.1103/PhysRevB.103.125411](https://doi.org/10.1103/PhysRevB.103.125411)

I. INTRODUCTION

Recently, non-Hermitian systems have attracted tremendous attention in the fields of condensed-matter physics and topological materials [1–12] since the non-Hermitian Hamiltonians are found to be appropriate for describing many systems, such as open systems [13–18], wave systems with gain and/or loss [19–25], etc. Specifically, the Su-Schrieffer-Heeger (SSH) model, with a simple mathematical form but rich topological phases, has been suggested to analytically elucidate the physical properties of non-Hermitian systems [26–30]. Previous works have reported novel topological behaviors in non-Hermitian SSH systems, such as exceptional points (EPs) under the periodic boundary condition (PBC) and the skin effect [26,31–33] under the open boundary condition (OBC). Physically, EPs, defined as the points where the eigenvalues and the corresponding eigenvectors coalesce [34,35], often lead to unconventional effects in non-Hermitian systems such as enhanced transmission through quantum dots for quantum resonances [36,37] and enhanced laser linewidth in a phonon laser [38]. The skin effect means exponential localization of continuum-spectrum eigenstates for both bulk and edge states at boundaries, which leads to the breakdown of the conventional bulk-boundary correspondence (BBC). As a result, the open boundary spectra manifest quite different from that of the PBC, and thus, the OBC systems cannot be described by the conventional Bloch band theory. Several attempts have been devoted to restoring the BBC and building the connection between topological invariants and the topological edge states such as the non-Bloch band theory

with quasimomentum of the complex value in a generalized Brillouin zone (GBZ) [31,39–41] and a semi-infinite system to demonstrate the topological origin of non-Hermitian skin effects [33,42].

Due to a mathematical equivalence between the Schrödinger equation in the non-Hermitian system and wave equations or linearized equations of motion in classical physics [43], there have been many attempts to realize the non-Hermitian physics in real systems, such as photonics system [44,45], the acoustics system [46], electrical circuits [47], mechanical systems [48], and exciton-polariton condensates [49,50]. Among them, the topological electric circuit simulation, which may be much easier to tune by changing the parameters of the circuit components than other implementations of topological phases, has been proved to be an effective approach to realize various topological phases, such as Weyl semimetals [47,51], nodal-line semimetals [52,53], fracton physics [54], non-Hermitian Majorana edge states [55], non-Hermitian high-order topological phases [56–58], and the four-dimensional topological phase [59]. However, the long-range nonreciprocal hoppings have not been realized in real systems, including the electric circuit system. In this work, we consider long-range nonreciprocal hoppings in a topoelectric realization with a periodic electric circuit composed of inductors, capacitors, and operational amplifiers. We propose to analyze the effect on the topological behaviors of adding long-range nonreciprocal hopping to the one-dimensional (1D) SSH model and to find the condition of the coexistence of topological edge states and skin effects in the non-Hermitian SSH model with long-range nonreciprocal hopping.

In this work, a non-Hermitian SSH model with long-range nonreciprocal hopping is considered to investigate the effects of different parameter conditions on the energy eigenvalue spectra and topological properties. We show two cases of EPs

*These authors contributed equally to this work.

†yurui@whu.edu.cn

‡zhangh@fudan.edu.cn

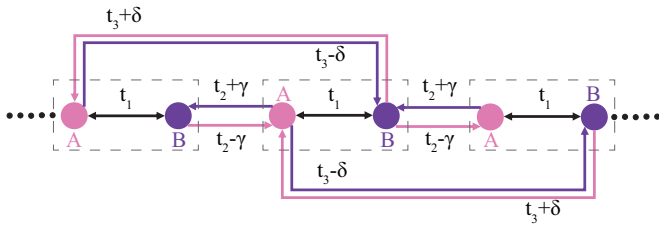


FIG. 1. Non-Hermitian SSH model. The dashed box indicates the unit cell.

in the first Brillouin zone classified by the number of EPs: A two-EP case and a four-EP case. For the former case, the conventional BBC is broken down, and the coexistence of topological edge states and skin effects can be observed in this model. The non-Bloch band theory is employed to construct the non-Bloch topological invariants in the GBZ and to investigate the non-Hermitian skin effect. However, for the latter case, the BBC exists, but the skin effect is excluded. Finally, we realize these properties by topoelectric simulations, which can be easily achieved by tuning the long-range nonreciprocal hoppings.

II. UNIQUE FEATURES IMPOSED BY NON-HERMITICITY

The non-Hermitian SSH model with long-range hopping under investigation is shown in Fig. 1, in which a unit cell contains two particles. The intracell interaction between the A and B particles within the same cell is reciprocal, while the intercell interactions between the A and B particles located within different cells are nonreciprocal, which forms the non-Hermitian system. The tight-binding Hamiltonian for this non-Hermitian SSH model can be written as

$$H(k) = d_x(k)\sigma_x + d_y(k)\sigma_y,$$

$$d_x(k) = t_1 + (t_2 + t_3) \cos k + i(\gamma + \delta) \sin k, \quad (1)$$

$$d_y(k) = (t_2 - t_3) \sin k + i(\delta - \gamma) \cos k,$$

where σ_i are the Pauli matrices and $t_{1,2,3}$, γ , and δ are hopping parameters, as shown in Fig. 1. Due to the absence of σ_z , this model has chiral symmetry, defined by $\sigma_z H(k) \sigma_z = -H(k)$. The Bloch eigenvalues of the Hamiltonian shown in Eq. (1) are obtained as $E_{\pm}(k) = \pm \sqrt{d_x^2(k) + d_y^2(k)}$. The eigenvalues coincide at the EPs [60,61], where $E_{\pm}(k) = 0$. When solving $E_{\pm}(k) = 0$, to ensure that the hopping parameters solved are real numbers, $d_x(k)$ and $d_y(k)$ should be purely real or purely

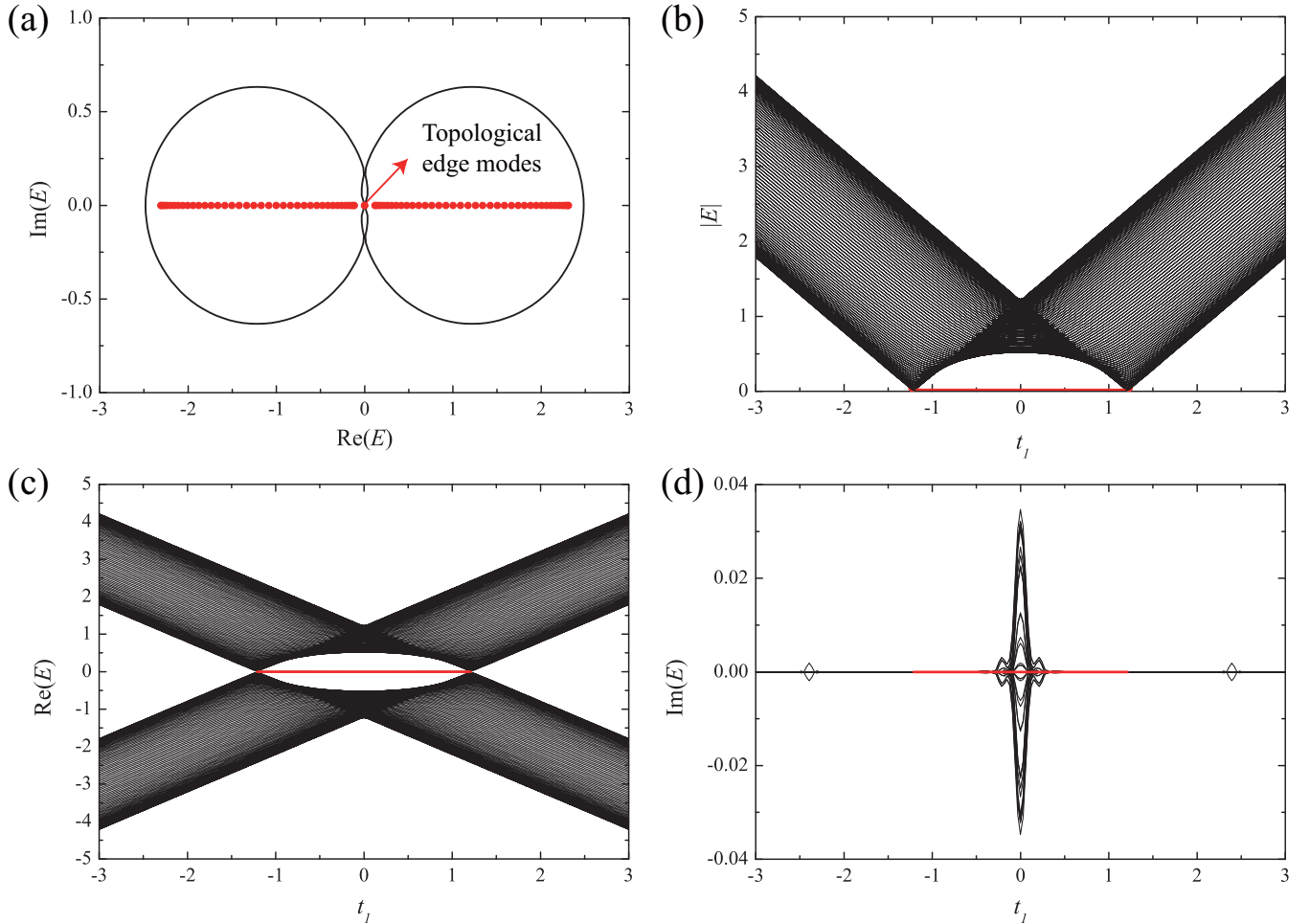


FIG. 2. (a) Energy spectra for systems with the PBC (solid curves) and the OBC (solid circles) with length $N = 80$ (unit cell). Parameter values are $t_1 = 1.1$, $t_2 = 1$, $t_3 = 0.4$, $\gamma = 0.5$, $\delta = 0.2$. (b) $|E|$ and (c) real and (d) imaginary parts of E of an open chain with $N = 160$ unit cells as a function of t_1 . The zero-mode line is shown in red. Parameter values are $t_2 = 1$, $t_3 = 0.4$, $\gamma = 0.5$, $\delta = 0.2$.

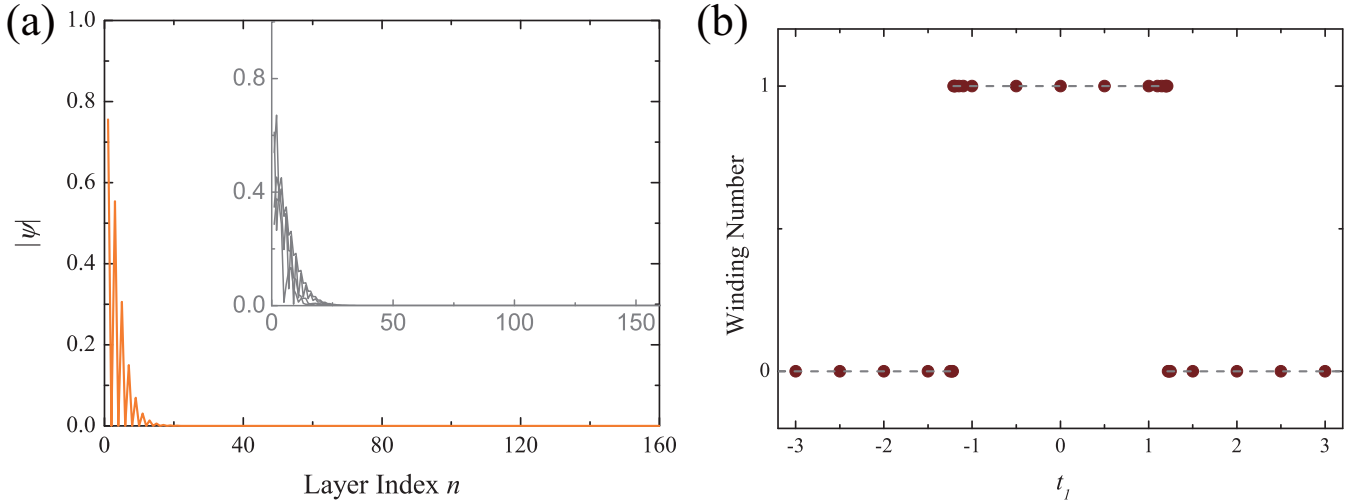


FIG. 3. (a) The absolute values of the amplitude from a zero-mode eigenstate (main figure) and bulk eigenstates (inset), showing the skin effect. (b) Winding number calculated by the GBZ approach. Parameter values are $t_2 = 1$, $t_3 = 0.4$, $\gamma = 0.5$, $\delta = 0.2$.

imaginary numbers on every k point. The EPs obtained can be summarized in two cases: (1) $k = 0$ when $t_1 = -(t_2 + t_3) \pm (\delta - \gamma)$ and $k = \pi$ when $t_1 = (t_2 + t_3) \pm (\delta - \gamma)$ and (2) $k = \arccos(\frac{t_1}{-2t_2 \pm 2\gamma})$ when $t_2 = t_3$ and $\gamma + \delta = 0$.

First, we take the parameter condition which satisfies case 1 into consideration. As shown in Fig. 2(a), the solid curves represent the energy spectra for systems with the PBC, while the spectrum of the Hamiltonian under the OBC H_{open} [solid circles in Fig. 2(a)] is obviously different from that of the PBC. The edge state zero mode can be identified in the spectrum, showing the topological origin of these parameters. Naturally, the phase transition points between topologically trivial and nontrivial phases under the same parameter condition should be solved out. For simplicity, if the hopping parameters satisfy $s = \sqrt{\frac{t_2 - \gamma}{t_2 + \gamma}} = \sqrt{\frac{t_3 - \delta}{t_3 + \delta}}$, we can construct a diagonal matrix $S = \text{diag}(1, 1, s, s, s^2, s^2, \dots, s^M, s^M)$ to transform H_{open} into a Hermitian matrix with a similarity transformation $S^{-1}H_{\text{open}}S$. Then the non-Hermitian model above become a Hermitian SSH model for $|t_2| > |\gamma|$ and $|t_3| > |\delta|$, with the hopping parameters $\tilde{t}_1 = t_1$, $\tilde{t}_2 = \sqrt{(t_2 - \gamma)(t_2 + \gamma)}$, $\tilde{t}_3 = \sqrt{(t_3 - \delta)(t_3 + \delta)}$. In k space, the Hamiltonian is

$$\tilde{H}(k) = [\tilde{t}_1 + (\tilde{t}_2 + \tilde{t}_3) \cos k] \sigma_x + [(\tilde{t}_2 - \tilde{t}_3) \sin k] \sigma_y. \quad (2)$$

For this Hermitian SSH model, we can obtain the phase transition points between topologically trivial and nontrivial phases in $\tilde{t}_1 = \pm[\tilde{t}_2 + \tilde{t}_3]$ [62], namely,

$$t_1 = \pm(\sqrt{t_2^2 - \gamma^2} + \sqrt{t_3^2 - \delta^2}). \quad (3)$$

With the hopping parameters in Fig. 2(a), Eq. (3) gives $t_1 \approx \pm 1.21$. Then we depict the open chain spectrum as a function of t_1 and observe the transition point at $t_1 \approx \pm 1.21$, which is consistent with Eq. (3). For $t_1 \propto (-1.21, 1.21)$, the energy spectra of the real-space Hamiltonian is gapless, while the energy spectrum of $H(k)$ may be gapped, indicating the breakdown of conventional bulk-boundary correspondence.

Furthermore, we can consider the eigenstate of the open boundary Hamiltonian H_{open} as $|\psi$

$[|\psi_{1,A}, \psi_{1,B}, \dots, \psi_{M,A}, \psi_{M,A}]^T$. So for the open boundary eigenstates $|\psi\rangle$ and $|\tilde{\psi}\rangle$ for H_{open} and \tilde{H} , respectively, it is obvious that $H_{\text{open}}|\psi\rangle = E|\psi\rangle$ equals $\tilde{H}|\tilde{\psi}\rangle = E|\tilde{\psi}\rangle$, with $|\psi\rangle = S|\tilde{\psi}\rangle$. Because \tilde{H} is a Hermitian SSH model, the eigenstates of H_{open} are exponentially localized on one side of the 1D open chain when $\gamma \neq 0$ and $\delta \neq 0$, as shown in Fig. 3(a), which is called the “non-Hermitian skin effect” [63]. In conclusion, for $t_1 \propto (-1.21, 1.21)$ in case 1, both topological edge states and the non-Hermitian skin effect exist in our model.

To further identify the non-Hermitian topological phases, the topological invariant needs to be calculated. Recent studies have proposed that, to describe the complex wave number \mathbf{k} in the 1D non-Hermitian SSH model, the Bloch phase factor $e^{i\mathbf{k}}$ can be replaced by $\beta = e^{i\mathbf{k}}$, which determines the generalized Brillouin zone C_β , a loop on the complex plane [31,39–41]. In this way, we can rewrite the non-Hermitian Hamiltonian $H(k)$ as $H(\beta)$ for our model, which is given as

$$\begin{aligned} H(\beta) &= h_+(\beta)\sigma_+ + h_-(\beta)\sigma_-, \\ h_+(\beta) &= t_1 + (t_2 - \gamma)\beta^{-1} + (t_3 + \delta)\beta, \\ h_-(\beta) &= t_1 + (t_2 + \gamma)\beta + (t_3 - \delta)\beta^{-1}, \end{aligned} \quad (4)$$

where $\sigma_{\pm} = (\sigma_x \pm i\sigma_y)/2$. Then we solve the eigenvalue equation $|H(\beta) - E| = 0$ to obtain $2N$ solutions. The middle two solutions β_N and β_{N+1} ($|\beta_1| \leq |\beta_2| \leq \dots \leq |\beta_N| \leq |\beta_{N+1}| \leq \dots \leq |\beta_{2N-1}| \leq |\beta_{2N}|$) constitute C_β under the condition $\beta_N = \beta_{N+1}$. According to the chiral symmetry, a Q matrix Q_β can be constructed from the eigenstates of $H(\beta)$. Finally, the winding number is defined as

$$w = \frac{i}{2\pi} \int_{C_\beta} dq q^{-1}(\beta), \quad (5)$$

where q_β is the off-diagonal element of Q_β . The winding number defined by Eq. (5) is calculated and shown in Fig. 3(a). More details are depicted in Appendix A. The changing point of w agrees with the transition point mentioned above.

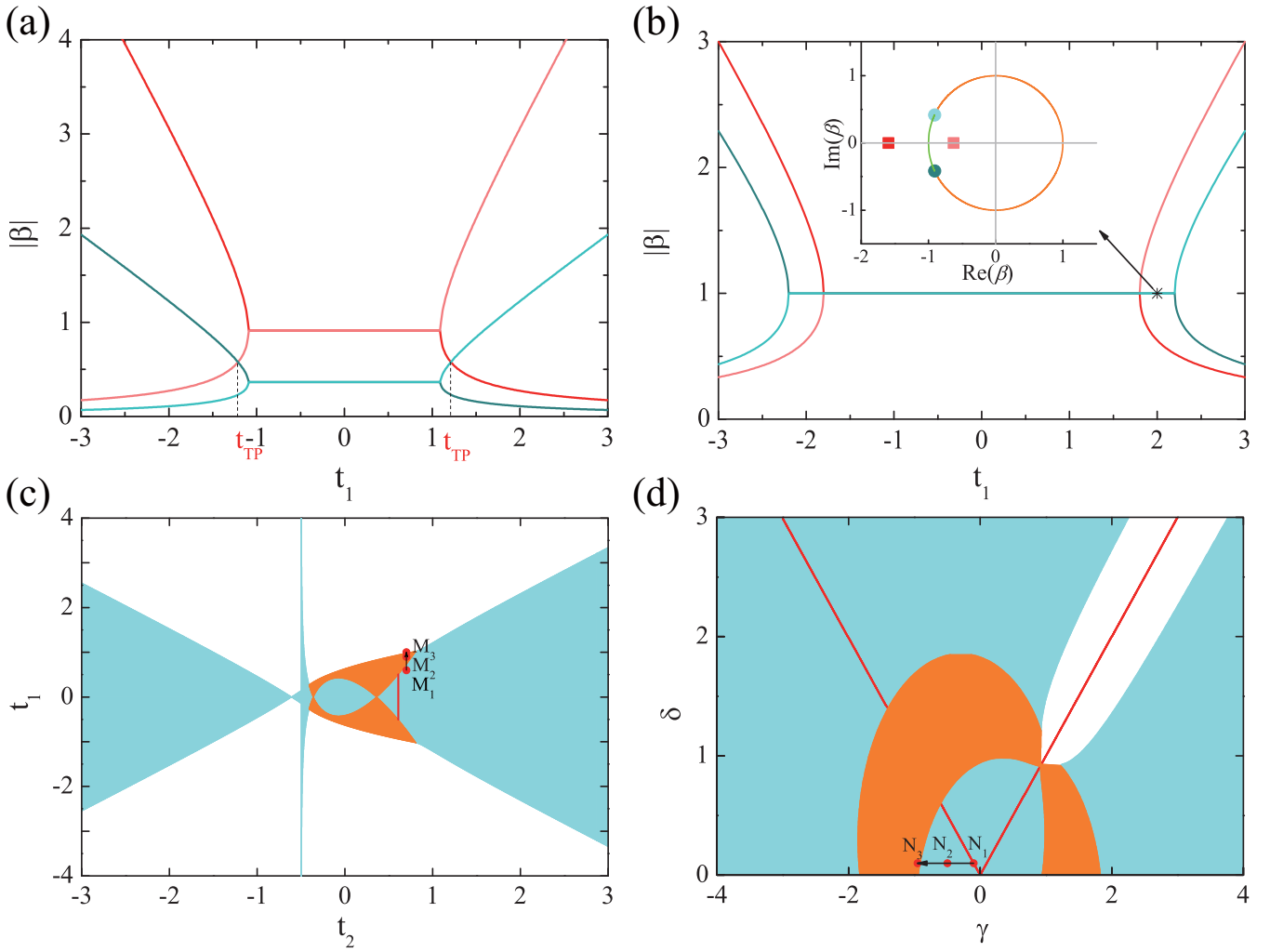


FIG. 4. (a) and (b) Illustration of how the ordering of $|\beta|$ determines the topological phase. $|\beta| = |a_1|, |a_2|, |b_1|, |b_2|$ are colored red, light red, cyan, and light cyan, respectively, with $t_2 = 1, t_3 = 0.4, \gamma = 0.5, \delta = 0.2$ in (a) and $t_2 = 1, t_3 = 1, \gamma = 0.1, \delta = -0.1$ in (b). The inset in (b) is the GBZ formed by complex-valued $|b_{1,2}|$ in the specified energy region at $t_1 = 2$. The orange and green regions represent that the energies are real and purely imaginary, respectively. $|\beta| = |a_1|, |a_2|, |b_1|, |b_2|$ are shown by a red square, a light red square, a cyan dot, and a light cyan dot, respectively. (c) Phase diagram on the t_1 - t_2 plane with $t_3 = 0.4, \gamma = 0.5, \delta = 0.2$. (d) Phase diagram on the δ - γ plane with $t_1 = 0.8, t_2 = 1, t_3 = 1$. The cyan region represents a topologically nontrivial system, and the orange region represents the TSM phase, while the white region and the red line represent a topologically trivial system. $M_{1,2,3}$ are three data points of different phases along the black arrow ($t_2 = 0.7$) in (c) with $t_1 = 0.6, 0.9, 1$, respectively. $N_{1,2,3}$ are three data points in (d) of different phases along the black arrow ($\delta = 0.1$) with $\gamma = -0.1, -0.5, -0.95$, respectively.

More generally, we can directly distinguish the topology of the given model by the ordering of the roots β_n at $E = 0$, which is consistent with the ordering of the spatial decay length of their corresponding eigenmodes [33]. First, we obtain the complex roots of $h_{+/-}(\beta)$, $a_{1,2} = \frac{-t_1 \pm \sqrt{t_1^2 - 4(t_2 - \gamma)(t_3 + \delta)}}{2(t_3 + \delta)}$ and $b_{1,2} = \frac{-t_1 \pm \sqrt{t_1^2 - 4(t_2 + \gamma)(t_3 - \delta)}}{2(t_2 + \gamma)}$, which constitute β_n . Second, $H(\beta)$ can be rewritten as [33]

$$H(\beta) = \begin{pmatrix} 0 & C_a \beta^{-q_a} \Pi_i^{p_a} (\beta - a_i) \\ C_b \beta^{-q_b} \Pi_i^{p_b} (\beta - b_i) & 0 \end{pmatrix}, \quad (6)$$

where $C_{a/b}$ is the normalization constant, $p_a = p_b = p = 2$, $q_a = q_b = q = 1$, and $r_a = r_b = p - q = 1$. According to Ref. [33], the topological criterion is expressed as follows: The first $(r_a + r_b)$ largest β_n 's can never be

composed of r_a members from a_i and r_b members from b_i . In other words, the largest two roots must be either $a_{1,2}$ or $b_{1,2}$ for the given model. We take cases 1 and 2 as examples to show the process of determining the range of hopping parameters. With the hopping parameters in Fig. 2, the absolute values of $a_{1,2}$ and $b_{1,2}$ changing with t_1 are shown in Fig. 4(a). When $|t_1| \leq 2\sqrt{(t_2 + \gamma)(t_3 - \delta)}$ [$|t_1| \leq 2\sqrt{(t_2 - \gamma)(t_3 + \delta)}$], $a_{1,2}$ ($b_{1,2}$) becomes complex, and its absolute value remains constant: $\sqrt{\frac{t_2 - \gamma}{t_3 + \delta}} (\sqrt{\frac{t_3 - \delta}{t_2 + \gamma}})$. When t_1 ($t_1 > 0$) is outside the above range, $|a_1|$ ($|b_1|$) monotonously decreases, while $|a_2|$ ($|b_2|$) monotonously increases. Thus, $|a_1|$ and $|b_2|$ meet at the phase transition point: $|t_{TP}| = \frac{t_2^2 - t_3^2 - \gamma^2 + \delta^2}{\sqrt{(t_2 - t_3)^2 - (\gamma - \delta)^2}} \approx 1.21$. However, for case 2, at $t_1 = 0$, we can obtain $t_2^2 - \gamma^2 = \pm(t_3^2 - \delta^2)$

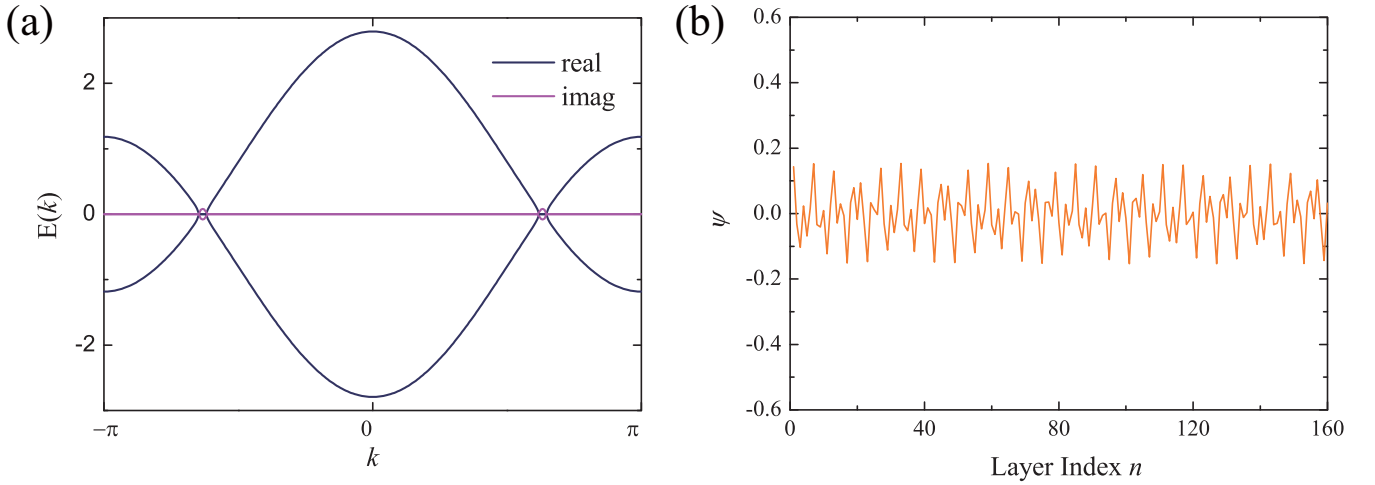


FIG. 5. (a) Energy spectra for systems with the PBC. (b) The amplitude values from a bulk eigenstate. Parameter values are $t_1 = 0.8$, $t_2 = 1$, $t_3 = 1$, $\gamma = 0.1$, $\delta = -0.1$.

from $|a_{1,2}| = |b_{1,2}|$. Under these conditions, if $t_1 > 0$, obviously, $|a_1| \leq |\sqrt{\frac{-(t_2-\gamma)}{(t_3+\delta)}}| = 1 \leq |a_2|$, and $|b_1| \leq |\sqrt{\frac{-(t_3-\delta)}{(t_2+\gamma)}}| = 1 \leq |b_2|$, which cannot satisfy the topological criterion, as shown in Fig. 4(b). Therefore, the system with the hopping parameters in case 2 cannot possess topological edge states.

Moreover, when we focus on the range of $1.8 < |t_1| < 2.2$, as shown in Fig. 4(b), a unique feature of the generalized Brillouin zone can be found. For example, at $t_1 = 2$ in Fig. 4(b), $|a_{1,2}|$ and $|b_{1,2}|$ correspond to the gap-closing points of $H(\beta)$, shown as squares and dots in the inset in Fig. 4(b), respectively. Because $|a_2| < |b_1| = |b_2| < |a_1|$ holds, the condition for the formation of the GBZ can be satisfied, and $|b_{1,2}|$ are on the GBZ. Hence, they are the exceptional points on the GBZ, and this feature is called a topological semimetal (TSM) phase with exceptional points in the GBZ [64]. Based on a similar analysis, we obtain the phase diagram on the t_1 - t_2 plane in Fig. 4(c) and the γ - δ plane in Fig. 4(d). The cyan areas represent the parameter range with topologically nontrivial properties, and hence, topological edge modes exist. The orange areas represent the TSM phase, which is an intermediate phase between a trivial insulator phase and a topologically nontrivial insulator phase in the GBZ. The hopping parameters in the white area and the red line lead to a topologically trivial system.

In case 2, the Hamiltonian is PT symmetric, where P is the parity operator and T is the time reversal operator, defined by $PTH T^{-1} P^{-1} = H$ ($P = \sigma_x$ and $T = K$, which denotes complex conjugation) [65]. As in the antilinear symmetry case, the eigenvectors of this Hamiltonian are either broken or unbroken. Therefore, the eigenenergies are either purely real or imaginary with the combination of the antilinear and chiral symmetries [27], which can be seen in Fig. 5(a). The solution to the Hamiltonian possesses four exceptional points in the first Brillouin zone. The bulk-boundary correspondence occurs in spite of the non-Hermiticity in this case. Furthermore, we choose a bulk eigenstate to plot the amplitude values in Fig. 5(b). Different from case 1, the Hamiltonian with $t_2 = t_3$

and $\gamma + \delta = 0$ possesses pseudo-Hermitian symmetry [i.e., $\sigma_x H^\dagger(k) \sigma_x^{-1} = H(k)$]. Thus, the middle two solutions to the non-Hermitian Hamiltonian $H(\beta)$, i.e., $|H(\beta) - E| = 0$, satisfy the condition of $|\beta_2| = |\beta_3| = 1$ [66], which is consistent with the numerical results, as shown in Fig. 4(b), leading to the real wave number k even under the OBC. Notably, the pseudo-Hermitian symmetry in non-Hermitian systems restores the delocalization of bulk wave functions [66]. Therefore, the eigenstate is not localized on the left end of the open chain, indicating that the non-Hermitian skin effect is excluded.

III. NON-HERMITIAN ELECTRICAL CIRCUIT LATTICE

In this section, to realize the non-Hermitian SSH model with long-range hopping, we construct a 1D electrical circuit lattice consisting of capacitors, inductors, and operational amplifiers [52,53,59]. The non-Hermitian effect is implemented by the operational amplifier, whose input consists of a noninverting input V_+ and an inverting input V_- and whose output is represented by V_{out} . These three parameters can be connected by the equation $V_{\text{out}} = A(V_+ - V_-)$, where A is the open-loop gain with a large value for an operational amplifier, amplifying the difference between the two inputs. $V_- = V_{\text{out}}$ is allowed when the inverting input is connected to the output, leading to $V_{\text{out}} = A(V_+ - V_{\text{out}}) \Rightarrow V_{\text{out}} = \frac{A}{A+1} V_+ \approx V_+$. Since no voltage crosses the inputs for an ideal operational amplifier, the input terminals show the characteristics of a short circuit, but there is no current between them. Based on the discussions above and Kirchoff's current law, we now can construct a circuit lattice corresponding to the tight-binding model, Eq. (1), which is shown in Fig. 6.

By mapping the tight-binding Hamiltonian to the circuit lattice, the hopping parameters correspond to the capacitor, the wave function corresponds to the voltage, and the eigenvalue corresponds to the resonance frequency. So that a tight-binding-like Hamiltonian can be derived from the

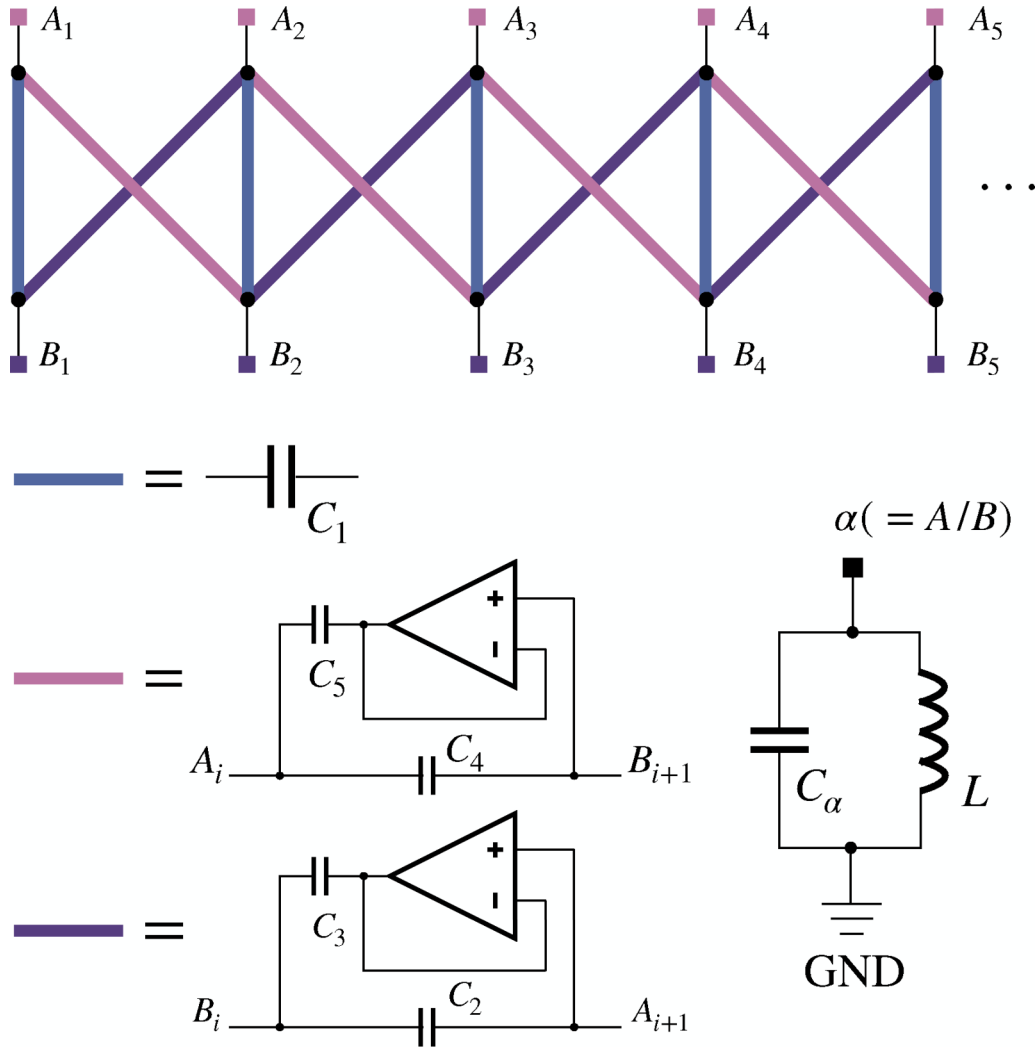


FIG. 6. A 1D non-Hermitian electrical circuit lattice consisting of operational amplifiers and capacitors with long-range hopping. C_i are capacitors. The non-Hermitian effect is implemented thanks to the operational amplifier, whose input consists of a noninverting input V_+ and an inverting input V_- and whose output is represented by V_{out} . $V_- = V_{out}$ is allowed when the inverting input is connected with the output.

Kirchhoff equations,

$$\begin{aligned}
 H(k) &= \varepsilon_s \sigma_0 + d_x(k) \sigma_x + d_y(k) \sigma_y, \\
 \varepsilon_s &= C_1 + C_2 + C_3 + C_4 + C_5 + C_G, \\
 d_x(k) &= -\left[C_1 + \left(C_2 + C_4 + \frac{C_3}{2} + \frac{C_5}{2} \right) \cos k \right. \\
 &\quad \left. + i \left(\frac{C_3}{2} + \frac{C_5}{2} \right) \sin k \right], \\
 d_y(k) &= -\left[\left(C_2 - C_4 + \frac{C_3}{2} - \frac{C_5}{2} \right) \sin k \right. \\
 &\quad \left. - i \left(\frac{C_3}{2} - \frac{C_5}{2} \right) \cos k \right]. \quad (7)
 \end{aligned}$$

The details of the derivation are given in Appendix B. Comparing Eq. (1) with Eq. (7), we obtain $t_1 = -C_1$, $t_2 = -(C_2 + \frac{C_3}{2})$, $t_3 = -(C_4 + \frac{C_5}{2})$, $\gamma = -\frac{C_3}{2}$, $\delta = -\frac{C_5}{2}$. Therefore, by tuning the values of capacitors, we can realize the topological phases mentioned before in the 1D non-Hermitian electrical circuit lattice with long-range hopping, such as the

$M_{1,2,3}$ phases. To realize the $N_{1,2,3}$ phases without negative capacitance, we need to make a little change to the circuit lattice: exchanging the input and output of the operational amplifier, as shown in Fig. 10. Finally, following the same derivation process in Appendix B, we obtain $t_1 = -C_1$, $t_2 = -(C_2 + \frac{C_3}{2})$, $t_3 = -(C_4 + \frac{C_5}{2})$, $\gamma = \frac{C_3}{2}$, $\delta = -\frac{C_5}{2}$.

IV. SIMULATION RESULTS

We carried out the circuit simulations on different phases, e.g., $M_{1,2,3}$ and $N_{1,2,3}$ in Figs. 4(c) and 4(d), which correspond to the topologically trivial phase, topological semimetal phase, and topologically nontrivial phase, respectively, for both the PBC and OBC. The voltage signals $V(r, t)$ of the $2N$ ($N = 40$) junctions in the real-space and time domain are extracted from the simulation results, and the amplitude of the eigenstates $V(f)$ can be calculated through the Fourier transformation. First, the dispersion spectra under the PBC for the $M_{1,2,3}$ and $N_{1,2,3}$ phases are under investigations. However, except for N_1 in case 2, for the topoelectric simulations for the other five phases under the PBC here, the influence

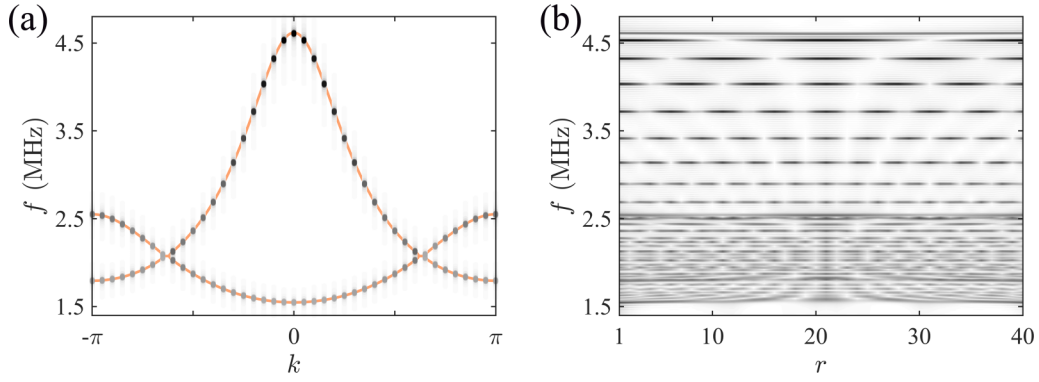


FIG. 7. (a) The simulation result for N_1 under the PBC. (b) The amplitude of the simulated eigenstates for N_1 under the PBC. The parameters are set as $L = 5.6 \mu H$, $C_G = 150 pF$, $C_1 = 240 pF$, $C_2 = 270 pF$, $C_3 = 60 pF$, $C_4 = 270 pF$, and $C_5 = 60 pF$ in the 1D circuit lattice with 40 cells.

of the negative imaginary part of the frequencies cannot be negligible, which causes serious divergency, finally leading to the unexpected dispersion spectra, e.g., the case of the M_1 phase, as shown in Fig. 11(a). The calculated dispersion spectra for the N_1 phase under the PBC from topoelectric simulations is shown in Fig. 7(a) as dots, which agree well with the dispersion calculated by models denoted by orange lines. Different from other phases, although the negative imaginary frequencies exist for the N_1 case under the PBC, the circuit system still remains stable, resulting from the protection of pseudo-Hermitian symmetry [66], described by $\sigma_x H^\dagger(k) \sigma_x^{-1} = H(k)$, since the eigenstates $(V_A(k), V_B(k))^T$ are always paired with $(-V_A(k), V_B(k))^T$ or $(V_A(k), -V_B(k))^T$. Furthermore, the circuit system with pseudo-Hermiticity is insensitive to the boundary conditions [66], which guarantees the stability of the system for the OBC as well. The frequency at the exceptional point for the N_1 phase under the PBC is obtained as 2.075 MHz from simulations, as shown in Fig. 7(a), which corresponds to a wave vector consistent with that calculated from models shown in Fig. 5(a). As shown in Fig. 7(b), only bulk states exist for the PBC in real space, and they are delocalized.

Second, the simulated eigenstates for all six phases under the OBC are shown in Fig. 8. Owing to the reality of OBC spectra, the voltage cannot diverge seriously in the finite time length, guaranteeing the stability of the circuit system. For the topologically nontrivial phases of the M_1 and N_2 phases, both the topological edge states and skin modes exist, which

are localized on one side of the 1D open chain, as shown in Figs. 8(a) and 8(e), manifesting the topological nontriviality and the breakdown of bulk-boundary correspondence, as mentioned above. The frequency of the topological edge states is obtained from simulations as 2.054 and 1.993 MHz for the M_1 and N_2 phases, respectively, which agree well with the model results. For the topologically trivial phase of the N_1 phase in case 2, the calculated eigenstates for the OBC from simulations shown in Fig. 8(d) indicate that the edge states do not exist and the bulk modes are delocalized and exhibit the topological triviality and the bulk-boundary correspondence, consistent with the aforementioned model results for case 2. For a general topologically trivial phase like the M_3 phase shown in Fig. 8(c), the edge states do not exist, but the bulk modes are localized. The M_2 and N_3 phases correspond to the TSM phase, and the circuit simulations for the OBC are shown in Figs. 8(b) and 8(f). The eigenstates obtained from simulations are localized at the edge and remain continuous over the frequency range, verifying that the energy spectrum under the OBC is gapless for the TSM phase. Different from the TSM phase, a general topologically trivial phase like the M_3 phase shown in Fig. 8(c) possesses an obvious separation at around $f = 1.885$ MHz.

V. CONCLUSIONS

In this work we have investigated the topological phase in the 1D non-Hermitian SSH model with long-range non-reciprocal hopping being considered. According to chiral symmetry, two cases of exceptional points exist: (1) two EPs located at $k = 0$ or $k = \pi$ and (2) four EPs when $t_2 = t_3$ and $\gamma + \delta = 0$. The former one shows the non-Hermitian skin effect, indicating the breakdown of the bulk-boundary correspondence. We also employed non-Bloch band theory to calculate the transition point and the topological invariant of the non-Hermitian SSH model in case 1 with the generalized Brillouin zone. However, the latter case is a topologically trivial case, and the non-Hermitian skin effect is excluded. Finally, we proposed electrical circuit simulations, which have the advantage of easily achieving and tuning long-range non-reciprocal hoppings, to realize these exotic topological phases, and the simulation results show consistency with the model results.

TABLE I. Detailed parameters for the simulation of $M_{1,2,3}$ and $N_{1,2,3}$.

| Capacitance (pF) | M_1 | M_2 | M_3 | N_1 | N_2 | N_3 |
|------------------|-------|-------|-------|-------|-------|-------|
| C_g | 150 | 150 | 150 | 150 | 150 | 150 |
| C_1 | 240 | 360 | 400 | 240 | 240 | 240 |
| C_2 | 80 | 80 | 80 | 270 | 150 | 15 |
| C_3 | 400 | 400 | 400 | 60 | 300 | 570 |
| C_4 | 80 | 80 | 80 | 270 | 270 | 270 |
| C_5 | 160 | 160 | 160 | 60 | 60 | 60 |
| C_A | 550 | 550 | 550 | 150 | 150 | 150 |
| C_B | 310 | 310 | 310 | 270 | 510 | 780 |

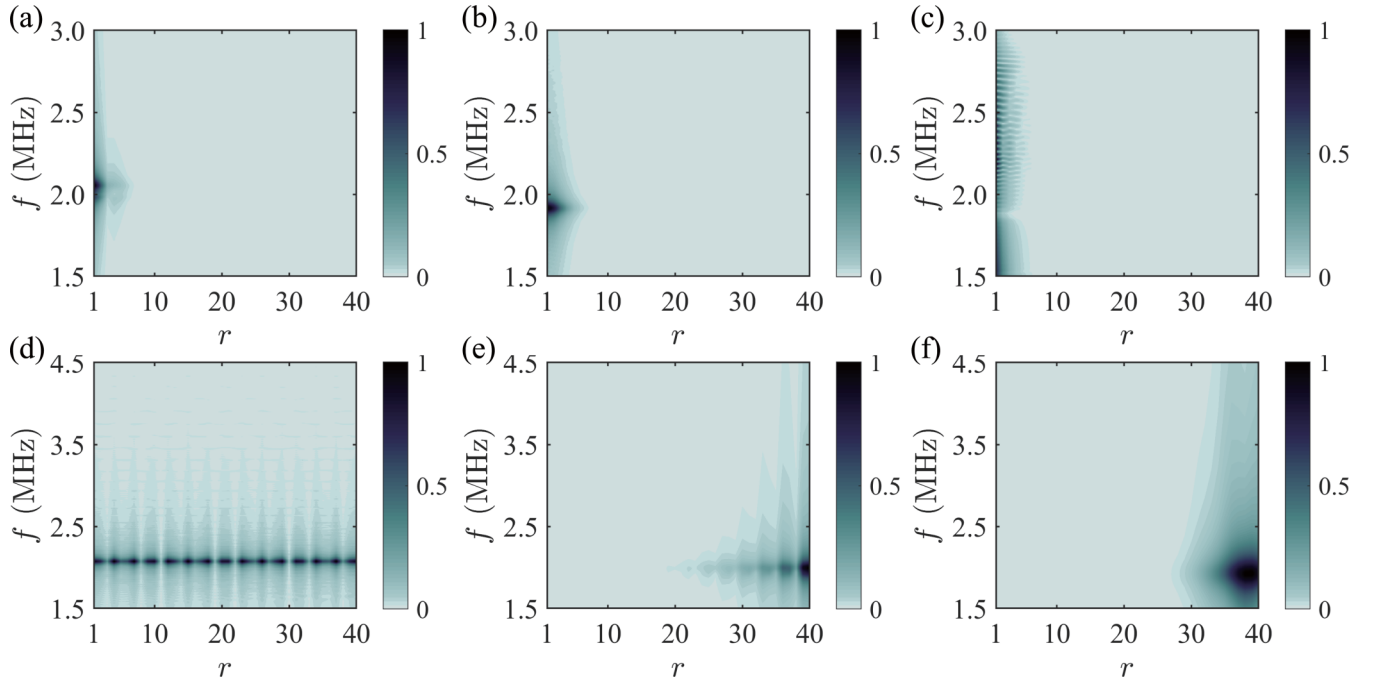


FIG. 8. The amplitude of the simulated eigenstates under the OBC. (a)–(c) correspond to phase sM_1 , M_2 , and M_3 . (d)–(f) correspond to phases N_1 , N_2 , and N_3 . The parameters are listed in Table I.

ACKNOWLEDGMENTS

This work is supported by the National Natural Science Foundation of China under Grants No. 11374063 and No. 11974082, the National Key Research and Development Program of China under Grant No. 2017YFA0303403, and the Shanghai Municipal Natural Science Foundation under Grant No. 19ZR1402900.

APPENDIX A: NON-BLOCH BAND THEORY

Considering the 1D non-Hermitian SSH model, if we replace the Bloch phase factor e^{ik} by $\beta = e^{ik}$, the non-Hermitian Hamiltonian $H(k)$ can be rewritten as $H(\beta)$:

$$\begin{aligned} H(\beta) &= h_+(\beta)\sigma_+ + h_-(\beta)\sigma_-, \\ h_+(\beta) &= t_1 + (t_2 - \gamma)\beta^{-1} + (t_3 + \delta)\beta, \\ h_-(\beta) &= t_1 + (t_2 + \gamma)\beta + (t_3 - \delta)\beta^{-1}, \end{aligned} \quad (\text{A1})$$

where $\sigma_{\pm} = (\sigma_x \pm i\sigma_y)/2$. Solving the eigenvalue equation $|H(\beta) - E| = 0$, we obtain

$$\begin{aligned} [t_1 + (t_2 - \gamma)\beta^{-1} + (t_3 + \delta)\beta][t_1 + (t_2 + \gamma)\beta + (t_3 - \delta)\beta^{-1}] \\ = E^2, \end{aligned} \quad (\text{A2})$$

which has four solutions, satisfying $|\beta_1| \leq |\beta_2| \leq |\beta_3| \leq |\beta_4|$. We plot $|\beta| - E$ curves in Fig. 9(a). The middle two solutions $\beta_{2,3}$ are what we care about. In the $E \rightarrow 0$ limit, $|\beta_2| = |\beta_3|$ can determine the transition point: $t_1 = 1.21$ for these parameters. In the common energy region, $|\beta_2| = |\beta_3|$ determines the generalized Brillouin zone (GBZ) C_β , which is a closed loop encircling the origin on the complex plane, and it is shown in Fig. 9(b).

Thanks to the GBZ approach, we can also calculate the winding number w of $H(\beta)$ by defining a Q matrix. First, the

right and left eigenstates of $H(\beta)$ can be written as

$$\begin{aligned} |u_R\rangle &= \frac{1}{\sqrt{2}} \begin{pmatrix} \frac{h_+}{\sqrt{h_+h_-}} \\ 1 \end{pmatrix}, \\ |\tilde{u}_R\rangle &= \frac{1}{\sqrt{2}} \begin{pmatrix} \frac{h_+}{\sqrt{h_+h_-}} \\ -1 \end{pmatrix}, \\ \langle u_L| &= \frac{1}{\sqrt{2}} \left(\frac{h_-}{\sqrt{h_+h_-}}, 1 \right), \\ \langle \tilde{u}_L| &= \frac{1}{\sqrt{2}} \left(\frac{h_-}{\sqrt{h_+h_-}}, -1 \right). \end{aligned} \quad (\text{A3})$$

The eigenvectors, $|u_R\rangle = \sigma_z |\tilde{u}_R\rangle$ and $\langle u_L| = \sigma_z \langle \tilde{u}_L|$, are guaranteed by chiral symmetry. The Q matrix is written as

$$\begin{aligned} Q(\beta) &= |u_R(\beta)\rangle \langle u_L(\beta)| - |\tilde{u}_R(\beta)\rangle \langle \tilde{u}_L(\beta)| \\ &= \begin{pmatrix} 0 & \frac{h_+}{\sqrt{h_+h_-}} \\ \frac{h_-}{\sqrt{h_+h_-}} & 0 \end{pmatrix}. \end{aligned} \quad (\text{A4})$$

Thus, we can obtain the off-diagonal element as $q = \frac{h_+}{\sqrt{h_+h_-}}$, and the winding number can be defined as

$$\begin{aligned} w &= \frac{i}{2\pi} \int_{C_\beta} dq q^{-1}(\beta) \\ &= \frac{i}{2\pi} \int_{C_\beta} d \ln q(\beta) \\ &= -\frac{1}{2\pi} [\arg q(\beta)]_{C_\beta} \\ &= -\frac{1}{2\pi} \frac{[\arg h_+(\beta) - \arg h_-(\beta)]_{C_\beta}}{2}. \end{aligned} \quad (\text{A5})$$

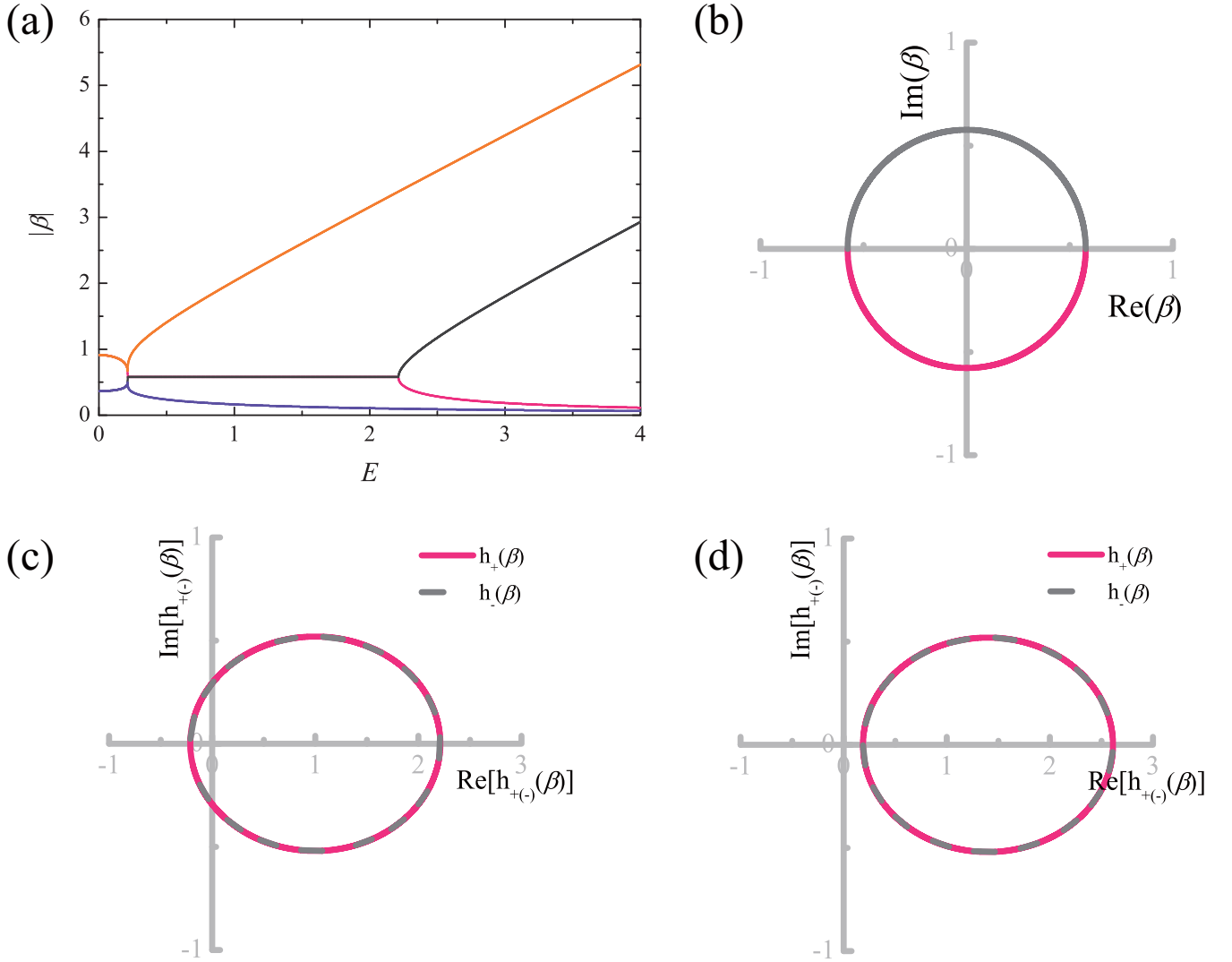


FIG. 9. (a) $|\beta|$ - E curves from Eq. (A2). $t_1 = 1$. (b) A closed loop C_β formed by complex-valued $\beta_{2,3}$. $t_1 = 1$. (c) and (d) The evolution loop of $h_{+/-}(\beta)$ on the complex plane with $t_1 = 1$ and $t_1 = 1.4$. Common parameter values are $t_2 = 1$, $t_3 = 0.4$, $\gamma = 0.5$, $\delta = 0.2$.

Therefore, the phase change in $h_{+/-}(\beta)$ along C_β determines the winding number w . We plot the evolution loop of $h_{+/-}(\beta)$ on the complex plane for different parameters, and it is shown

in Figs. 9(c) and 9(d). When two loops simultaneously enclose the origin, w takes a nonzero value [$t_1 = 1$ in Fig. 9(c)]. However, w is zero when neither of the two loops goes around the origin [$t_1 = 1.4$ in Fig. 9(d)].

APPENDIX B: DETAILS OF THE DERIVATION OF EQUATION (7)

According to Kirchhoff's current law, the currents flowing through the A and B nodes at $R = 0$ in Fig. 10 are given as

$$\begin{aligned}
 I_{A,0} &= j\omega C_1(V_{B,0} - V_{A,0}) + j\omega C_2(V_{B,-a} - V_{A,0}) + j\omega(C_4 + C_5)(V_{B,a} - V_{A,0}) \\
 &\quad + j\omega(C_G + C_3)(0 - V_{A,0}) + \frac{1}{j\omega L}(0 - V_{A,0}), \\
 I_{B,0} &= j\omega C_1(V_{A,0} - V_{B,0}) + j\omega(C_2 + C_3)(V_{A,a} - V_{B,0}) + j\omega C_4(V_{A,-a} - V_{B,0}) \\
 &\quad + j\omega(C_G + C_5)(0 - V_{B,0}) + \frac{1}{j\omega L}(0 - V_{B,0}),
 \end{aligned} \tag{B1}$$

where $V_{A/B,\mathbf{R}}$ are the voltages. Since the 1D non-Hermitian SSH model has transformation invariant symmetry, the voltage follows the Bloch theorem: $V(r + \mathbf{R}) = e^{i\mathbf{kR}}V(r)$. Kirchhoff's current law requires $I_{A,0}$ and $I_{B,0}$ to be zero. Thus, the above

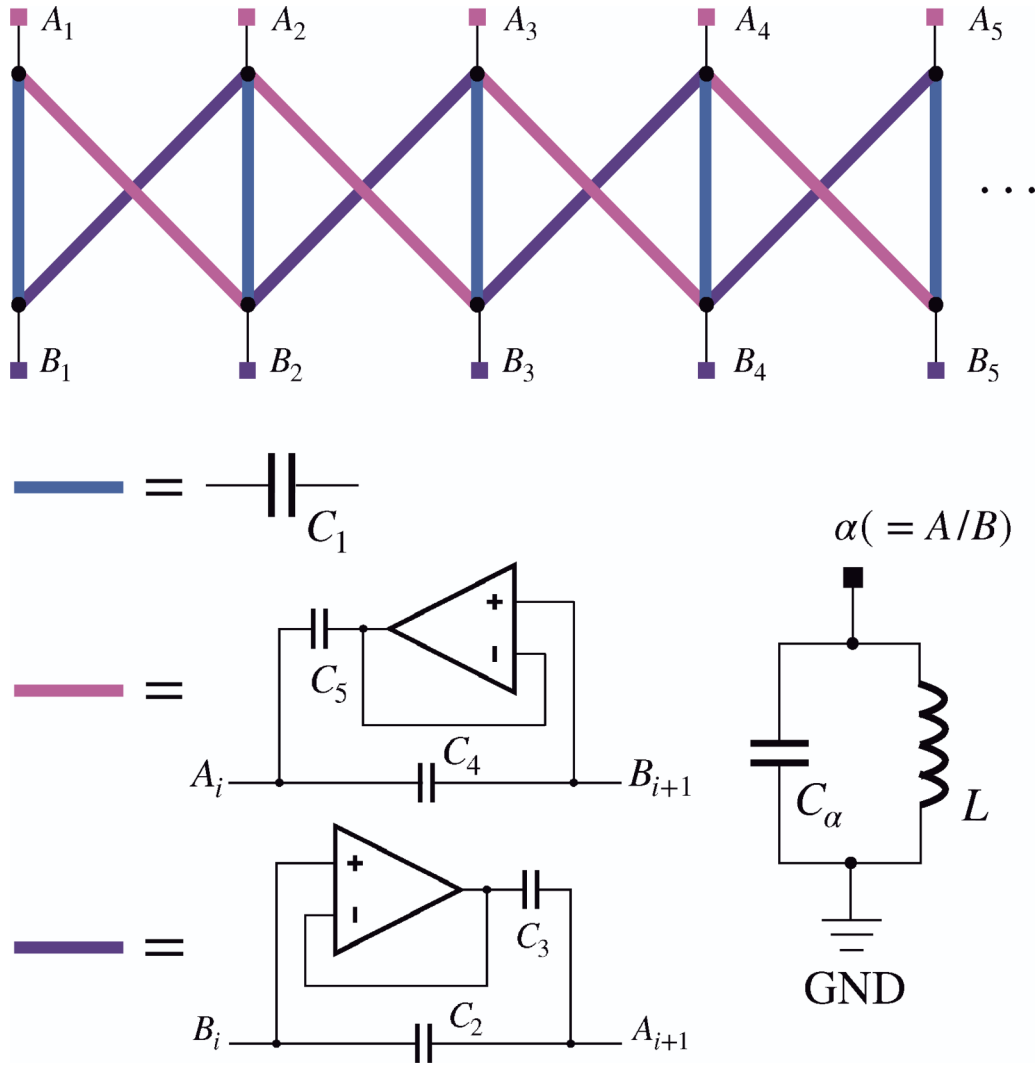


FIG. 10. A 1D non-Hermitian electrical circuit lattice consisting of operational amplifiers and capacitors with long-range hopping in the case $N_{1,2,3}$.

equations can be written in matrix form (supposing a to be 1),

$$\begin{bmatrix} (C_1 + C_2 + C_3 + C_4 + C_5 + C_G) & -[C_1 + C_2 e^{-ik} + (C_4 + C_5) e^{ik}] \\ -[C_1 + (C_2 + C_3) e^{ik} + C_4 e^{-ik}] & (C_1 + C_2 + C_3 + C_4 + C_5 + C_G) \end{bmatrix} \begin{bmatrix} V_{A,0} \\ V_{B,0} \end{bmatrix} = \frac{1}{\omega^2 L} \begin{bmatrix} V_{A,0} \\ V_{B,0} \end{bmatrix}. \quad (\text{B2})$$

Finally, we rewrite the matrix in terms of the Pauli matrices, which is given in the main text as Eq. (7).

APPENDIX C: SIMULATION DETAILS

The values of capacitors for the $M_{1,2,3}$ and $N_{1,2,3}$ phases are listed in Table I. For $M_{1,2,3}$ under the OBC, the source is placed to the left of the circuit lattice, while for $N_{1,2,3}$ under the OBC, the source is placed on the right side. The total time length of the simulation is set to $40 \mu\text{s}$ for the phases above except N_3 ($12 \mu\text{s}$). The time step is set to 10 ns, and the frequency step is set to 1 kHz when operating the Fourier transformation.

For N_1 in case 2 under the PBC, the source can be placed at any position, and the time length is set to $40 \mu\text{s}$ as well. The simulation results for M_1 under the PBC are shown in Fig. 11(a), where the simulated dispersion cannot correspond to the model dispersion and exhibit serious divergence due to the exclusion of pseudo-Hermitian symmetry. For example, at $k = -0.943$, the peak frequency is simulated to be 2.608 MHz, which is consistent with the model results, but another resonant frequency, 1.670 MHz, is excluded.

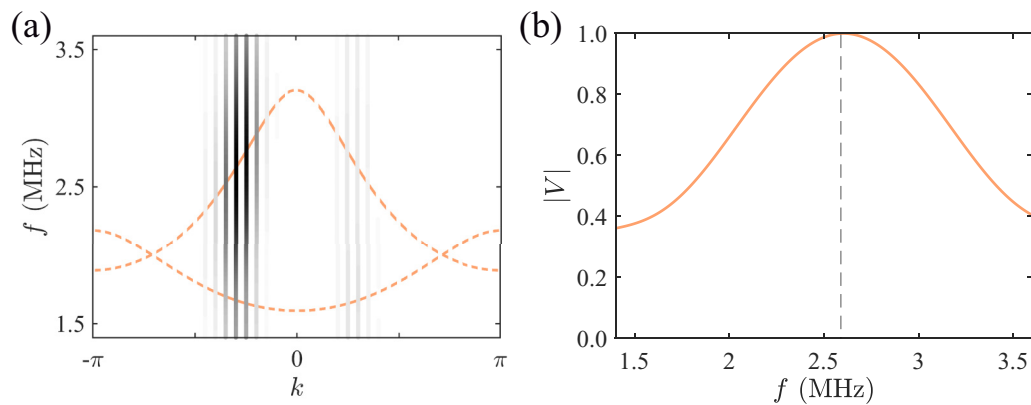


FIG. 11. The simulation results for M_1 under the PBC. The parameters are listed in Table I.

- [1] C. M. Bender and S. Boettcher, Real Spectra in Non-Hermitian Hamiltonians Having \mathcal{PT} Symmetry, *Phys. Rev. Lett.* **80**, 5243 (1998).
- [2] R. El-Ganainy, K. G. Makris, M. Khajavikhan, Z. H. Musslimani, S. Rotter, and D. N. Christodoulides, Non-Hermitian physics and \mathcal{PT} symmetry, *Nat. Phys.* **14**, 11 (2018).
- [3] H. Shen, B. Zhen, and L. Fu, Topological Band Theory for Non-Hermitian Hamiltonians, *Phys. Rev. Lett.* **120**, 146402 (2018).
- [4] Z. Gong, Y. Ashida, K. Kawabata, K. Takasan, S. Higashikawa, and M. Ueda, Topological Phases of Non-Hermitian Systems, *Phys. Rev. X* **8**, 031079 (2018).
- [5] Y. C. Hu and T. L. Hughes, Absence of topological insulator phases in non-Hermitian- \mathcal{PT} -symmetric Hamiltonians, *Phys. Rev. B* **84**, 153101 (2011).
- [6] K. Esaki, M. Sato, K. Hasebe, and M. Kohmoto, Edge states and topological phases in non-Hermitian systems, *Phys. Rev. B* **84**, 205128 (2011).
- [7] T. Rakovszky, J. K. Asbóth, and A. Alberti, Detecting topological invariants in chiral symmetric insulators via losses, *Phys. Rev. B* **95**, 201407(R) (2017).
- [8] D. Leykam, K. Y. Bliokh, C. Huang, Y. D. Chong, and F. Nori, Edge Modes, Degeneracies, and Topological Numbers in Non-Hermitian Systems, *Phys. Rev. Lett.* **118**, 040401 (2017).
- [9] A. Ghatak and T. Das, New topological invariants in non-Hermitian systems, *J. Phys.: Condens. Matter* **31**, 263001 (2019).
- [10] B. Zhu, R. Lü, and S. Chen, \mathcal{PT} symmetry in the non-Hermitian Su-Schrieffer-Heeger model with complex boundary potentials, *Phys. Rev. A* **89**, 062102 (2014).
- [11] L. Jin and Z. Song, Bulk-boundary correspondence in a non-Hermitian system in one dimension with chiral inversion symmetry, *Phys. Rev. B* **99**, 081103(R) (2019).
- [12] S.-D. Liang and G.-Y. Huang, Topological invariance and global Berry phase in non-Hermitian systems, *Phys. Rev. A* **87**, 012118 (2013).
- [13] H. J. Carmichael, Quantum Trajectory Theory for Cascaded Open Systems, *Phys. Rev. Lett.* **70**, 2273 (1993).
- [14] I. Rotter, A non-Hermitian Hamilton operator and the physics of open quantum systems, *J. Phys. A* **42**, 153001 (2009).
- [15] Y. Choi, S. Kang, S. Lim, W. Kim, J.-R. Kim, J.-H. Lee, and K. An, Quasieigenstate Coalescence in an Atom-Cavity Quantum Composite, *Phys. Rev. Lett.* **104**, 153601 (2010).
- [16] T. E. Lee and C.-K. Chan, Heralded Magnetism in Non-Hermitian Atomic Systems, *Phys. Rev. X* **4**, 041001 (2014).
- [17] K. G. Makris, R. El-Ganainy, D. N. Christodoulides, and Z. H. Musslimani, Beam Dynamics in \mathcal{PT} Symmetric Optical Lattices, *Phys. Rev. Lett.* **100**, 103904 (2008).
- [18] H. Cao and J. Wiersig, Dielectric microcavities: Model systems for wave chaos and non-Hermitian physics, *Rev. Mod. Phys.* **87**, 61 (2015).
- [19] A. Regensburger, C. Bersch, M.-A. Miri, G. Onishchukov, D. N. Christodoulides, and U. Peschel, Parity-time synthetic photonic lattices, *Nature (London)* **488**, 167 (2012).
- [20] L. Lu, J. D. Joannopoulos, and M. Soljačić, Topological photonics, *Nat. Photon.* **8**, 821 (2014).
- [21] S. Malzard, C. Poli, and H. Schomerus, Topologically Protected Defect States in Open Photonic Systems with Non-Hermitian Charge-Conjugation and Parity-Time Symmetry, *Phys. Rev. Lett.* **115**, 200402 (2015).
- [22] M. Pan, H. Zhao, P. Miao, S. Longhi, and L. Feng, Photonic zero mode in a non-Hermitian photonic lattice, *Nat. Commun.* **9**, 1308 (2018).
- [23] S. Weimann, M. Kremer, Y. Plotnik, Y. Lumer, S. Nolte, K. G. Makris, M. Segev, M. C. Rechtsman, and A. Szameit, Topologically protected bound states in photonic parity-time-symmetric crystals, *Nat. Mater.* **16**, 433 (2016).
- [24] T. Gao, E. Estrecho, K. Y. Bliokh, T. C. H. Liew, M. D. Fraser, S. Brodbeck, M. Kamp, C. Schneider, S. Höfling, Y. Yamamoto, F. Nori, Y. S. Kivshar, A. G. Truscott, R. G. Dall, and E. A. Ostrovskaya, Observation of non-Hermitian degeneracies in a chaotic exciton-polariton billiard, *Nature (London)* **526**, 554 (2015).
- [25] S. Longhi, Bloch Oscillations in Complex Crystals with \mathcal{PT} Symmetry, *Phys. Rev. Lett.* **103**, 123601 (2009).
- [26] F. K. Kunst, E. Edvardsson, J. C. Budich, and E. J. Bergholtz, Biorthogonal Bulk-Boundary Correspondence in Non-Hermitian Systems, *Phys. Rev. Lett.* **121**, 026808 (2018).
- [27] S. Lieu, Topological phases in the non-Hermitian Su-Schrieffer-Heeger model, *Phys. Rev. B* **97**, 045106 (2018).
- [28] S. Longhi, Probing non-Hermitian skin effect and non-Bloch phase transitions, *Phys. Rev. Res.* **1**, 023013 (2019).
- [29] C. Yuce, Stable topological edge states in a non-Hermitian four-band model, *Phys. Rev. A* **98**, 012111 (2018).

- [30] H. Jiang, C. Yang, and S. Chen, Topological invariants and phase diagrams for one-dimensional two-band non-Hermitian systems without chiral symmetry, *Phys. Rev. A* **98**, 052116 (2018).
- [31] S. Yao and Z. Wang, Edge States and Topological Invariants of Non-Hermitian Systems, *Phys. Rev. Lett.* **121**, 086803 (2018).
- [32] F. Song, S. Yao, and Z. Wang, Non-Hermitian Skin Effect and Chiral Damping in Open Quantum Systems, *Phys. Rev. Lett.* **123**, 170401 (2019).
- [33] C. H. Lee and R. Thomale, Anatomy of skin modes and topology in non-Hermitian systems, *Phys. Rev. B* **99**, 201103(R) (2019).
- [34] M. V. Berry, Physics of nonhermitian degeneracies, *Czech. J. Phys.* **54**, 1039 (2004).
- [35] W. D. Heiss, Exceptional points of non-Hermitian operators, *J. Phys. A* **37**, 2455 (2004).
- [36] M. Avinun-Kalish, M. Heiblum, O. Zarchin, D. Mahalu, and V. Umansky, Crossover from ‘mesoscopic’ to ‘universal’ phase for electron transmission in quantum dots, *Nature (London)* **436**, 529 (2005).
- [37] A. Levy Yeyati and M. Büttiker, Scattering phases in quantum dots: An analysis based on lattice models, *Phys. Rev. B* **62**, 7307 (2000).
- [38] J. Zhang, B. Peng, S. K. Özdemir, K. Pichler, D. O. Krimer, G. Zhao, F. Nori, Y. Liu, S. Rotter, and L. Yang, A phonon laser operating at an exceptional point, *Nat. Photon.* **12**, 479 (2018).
- [39] S. Yao, F. Song, and Z. Wang, Non-Hermitian Chern Bands, *Phys. Rev. Lett.* **121**, 136802 (2018).
- [40] F. Song, S. Yao, and Z. Wang, Non-Hermitian Topological Invariants in Real Space, *Phys. Rev. Lett.* **123**, 246801 (2019).
- [41] K. Yokomizo and S. Murakami, Non-Bloch Band Theory of Non-Hermitian Systems, *Phys. Rev. Lett.* **123**, 066404 (2019).
- [42] N. Okuma, K. Kawabata, K. Shiozaki, and M. Sato, Topological Origin of Non-Hermitian Skin Effects, *Phys. Rev. Lett.* **124**, 086801 (2020).
- [43] Y. Ashida, Z. Gong, and M. Ueda, Non-Hermitian physics, *arXiv:2006.01837*.
- [44] C. E. Rüter, K. G. Makris, R. El-Ganainy, D. N. Christodoulides, M. Segev, and D. Kip, Observation of parity–time symmetry in optics, *Nat. Phys.* **6**, 192 (2010).
- [45] A. Guo, G. J. Salamo, D. Duchesne, R. Morandotti, M. Volatier-Ravat, V. Aimez, G. A. Siviloglou, and D. N. Christodoulides, Observation \mathcal{PT} -Symmetry Breaking in Complex Optical Potentials, *Phys. Rev. Lett.* **103**, 093902 (2009).
- [46] S. A. Cummer, J. Christensen, and A. Alù, Controlling sound with acoustic metamaterials, *Nat. Rev. Mater.* **1**, 16001 (2016).
- [47] C. H. Lee, S. Imhof, C. Berger, F. Bayer, J. Brehm, L. W. Molenkamp, T. Kiessling, and R. Thomale, Topoelectrical circuits, *Commun. Phys.* **1**, 39 (2018).
- [48] K. Bertoldi, V. Vitelli, J. Christensen, and M. van Hecke, Flexible mechanical metamaterials, *Nat. Rev. Mater.* **2**, 17066 (2017).
- [49] H. Deng, H. Haug, and Y. Yamamoto, Exciton-polariton Bose-Einstein condensation, *Rev. Mod. Phys.* **82**, 1489 (2010).
- [50] C. Schneider, K. Winkler, M. D. Fraser, M. Kamp, Y. Yamamoto, E. A. Ostrovskaya, and S. Höfling, Exciton-polariton trapping and potential landscape engineering, *Rep. Prog. Phys.* **80**, 016503 (2016).
- [51] Y. Lu, N. Jia, L. Su, C. Owens, G. Juzeliūnas, D. I. Schuster, and J. Simon, Probing the Berry curvature and Fermi arcs of a Weyl circuit, *Phys. Rev. B* **99**, 020302(R) (2019).
- [52] K. Luo, J. Feng, Y. X. Zhao, and R. Yu, Nodal manifolds bounded by exceptional points on non-Hermitian honeycomb lattices and electrical-circuit realizations, *arXiv:1810.09231*.
- [53] K. Luo, R. Yu, and H. Weng, Topological nodal states in circuit lattice, *Research (Washington, DC)* **2018**, 1 (2018).
- [54] M. Pretko, Electric circuit realizations of fracton physics, *Phys. Rev. B* **100**, 245103 (2019).
- [55] M. Ezawa, Braiding of Majorana-like corner states in electric circuits and its non-Hermitian generalization, *Phys. Rev. B* **100**, 045407 (2019).
- [56] S. Imhof, C. Berger, F. Bayer, J. Brehm, L. W. Molenkamp, T. Kiessling, F. Schindler, C. H. Lee, M. Greiter, T. Neupert, and R. Thomale, Topoelectrical-circuit realization of topological corner modes, *Nat. Phys.* **14**, 925 (2018).
- [57] M. Ezawa, Higher-order topological electric circuits and topological corner resonance on the breathing kagome and pyrochlore lattices, *Phys. Rev. B* **98**, 201402(R) (2018).
- [58] M. Ezawa, Non-Hermitian higher-order topological states in nonreciprocal and reciprocal systems with their electric-circuit realization, *Phys. Rev. B* **99**, 201411(R) (2019).
- [59] R. Yu, Y. X. Zhao, and A. P. Schnyder, 4D spinless topological insulator in a periodic electric circuit, *Natl. Sci. Rev.* **7**, 1288 (2020).
- [60] W. D. Heiss, The physics of exceptional points, *J. Phys. A* **45**, 444016 (2012).
- [61] T. Stehmann, W. D. Heiss, and F. G. Scholtz, Observation of exceptional points in electronic circuits, *J. Phys. A* **37**, 7813 (2004).
- [62] M. Maffei, A. Dauphin, F. Cardano, M. Lewenstein, and P. Massignan, Topological characterization of chiral models through their long time dynamics, *New J. Phys.* **20**, 013023 (2018).
- [63] Y. Xiong, Why does bulk boundary correspondence fail in some non-Hermitian topological models, *J. Phys. Commun.* **2**, 035043 (2018).
- [64] K. Yokomizo and S. Murakami, Topological semimetal phase with exceptional points in one-dimensional non-Hermitian systems, *Phys. Rev. Res.* **2**, 043045 (2020).
- [65] P. D. Mannheim, Advancing the case for \mathcal{PT} symmetry – The Hamiltonian is always \mathcal{PT} symmetric, *arXiv:1506.08432*.
- [66] K. Kawabata, K. Shiozaki, M. Ueda, and M. Sato, Symmetry and Topology in Non-Hermitian Physics, *Phys. Rev. X* **9**, 041015 (2019).